

Characterization of fracture in topology-optimized bioinspired networksChantal Nguyen¹,[✉] Darin Peetz,² Ahmed E. Elbanna,² and Jean M. Carlson^{1,*}¹*Department of Physics, University of California, Santa Barbara, Santa Barbara, California 93106, USA*²*Department of Civil and Environmental Engineering, University of Illinois at Urbana–Champaign, Urbana, Illinois 61801, USA*

(Received 19 July 2019; revised manuscript received 4 September 2019; published 2 October 2019)

Designing strong and robust bioinspired structures requires an understanding of how function arises from the architecture and geometry of materials found in nature. We draw from trabecular bone, a lightweight bone tissue that exhibits a complex, anisotropic microarchitecture, to generate networked structures using multiobjective topology optimization. Starting from an identical volume, we generate multiple different models by varying the objective weights for compliance, surface area, and stability. We examine the relative effects of these objectives on how resultant models respond to simulated mechanical loading and element failure. We adapt a network-based method developed initially in the context of modeling trabecular bone to describe the topology-optimized structures with a graph-theoretical framework, and we use community detection to characterize locations of fracture. This complementary combination of computational methods can provide valuable insights into the strength of bioinspired structures and mechanisms of fracture.

DOI: [10.1103/PhysRevE.100.042402](https://doi.org/10.1103/PhysRevE.100.042402)**I. INTRODUCTION**

Understanding the relationships between architecture and function in biological materials is key to engineering bioinspired structures for strength and resilience. Materials found in nature must be spatially arranged to withstand repeated loading while facilitating various biological functions. In this paper, we use multiobjective topology optimization, finite-element modeling, and network science methods to generate and analyze a range of structures with varying emphases placed on maximizing stiffness, perimeter, and stability. We explore how differently weighting these objectives influences robustness and resistance of these structures to failure.

The bioinspired structures we develop in this paper are motivated by the challenge of reverse-engineering trabecular bone, a type of bone tissue that consists of an interconnected network of small struts called trabeculae. Its porous structure allows it to be lightweight, though it is weaker than the other type of bone tissue, cortical bone, which is hard, dense, and shell-like. Trabecular bone has roughly ten times the surface area of cortical bone. The pores in trabecular bone hold bone marrow, nerves, and blood vessels, and the increased surface area facilitates bone resorption and remodeling. This trade-off between the pore distribution and strength drives our choice of objectives in constructing structures guided by the emergent properties of vertebral trabecular bone.

Continuum topology optimization is a method that, given a set of objectives and constraints, optimizes the distribution of material within a domain [1]. We are motivated to use topology optimization to generate bone-inspired structures by the premise of Wolff's law [2]. Wolff's law states that, over time, trabecular bone remodels its architecture to adapt to the loads it is regularly subjected to. That is, it will

“self-optimize” itself into a structure that is more stiff along the primary loading directions. Analogously, multiobjective topology optimization starts from an initial density distribution, applies specified loads that in our case represent uniaxial loading in vertebrae, and minimizes a weighted sum of objective functions to achieve a desired architecture. Here the objective functions represent compliance (inverse stiffness), perimeter [the two-dimensional (2D) analog of surface area], and stability. Conceptually speaking, we assume that real bone is the outcome of a biological optimization procedure, but the quantities being optimized are unknown. While the topology-optimized structures are not intended to mimic bone, in isolating material properties associated with bone and varying the weights of corresponding objective functions, we examine how the relative weighting impacts overall toughness and robustness to failure.

The topology-optimized structures are disordered planar networks. We extract from them graph models consisting of edges representing struts (trabeculae), joined together at nodes that correspond to the branch points where the struts meet. This allows us to extract topological metrics that quantify the architecture of the network. This network-based method adapts the modeling approach developed by Mondal *et al.* [3] which modeled real human trabecular bone from micro-computed tomography images.

We analyze the mechanical response of the topology-optimized networks by converting the networks to finite-element models in which each edge is represented by a beam. We simulate compressive loading and failure in the beam-element models, and we investigate mechanics at scales ranging from individual beams to the entire network. In combining these computational methods, many of which have seen limited application to trabecular bone and bone-inspired materials, we relate the mechanics of bonelike structures to their architecture and identify how topology informs fracture. Our results inform the development and

*carlson@ucsb.edu

design of bioinspired networked structures that are robust and strong.

II. MULTI-OBJECTIVE TOPOLOGY OPTIMIZATION

The topology optimization process begins by assuming an initial two-dimensional density distribution on a discretized uniform grid of elements and then iteratively (1) performs a finite-element analysis step that simulates mechanical deformation, (2) carries out a gradient-based optimization step that updates the density distribution, and (3) evaluates the objective until convergence [4]. Three objectives were used: compliance (inverse stiffness) minimization, perimeter maximization, and stability (critical buckling load) maximization. The objective functions are combined as a weighted sum to form a single objective function that is evaluated in the iterative optimization procedure. Adjusting the weights of each objective function can result in highly variable topologies.

Each element has a density that can take on any value between 0 (void) and 1 (solid), but intermediate values are penalized using the solid isotropic material with penalization model (SIMP) [1] to ensure that the result contains binary density values. We include an area constraint in the optimization problem so that the total area of each generated structure is effectively constant. While the topology optimization method developed here is limited to two-dimensional structures, it can be generalized to three dimensions, albeit with a higher computational cost.

The most basic topology optimization problem is that of minimizing compliance (weights of perimeter and stability functions are set to zero) with an area constraint. The topology optimization problem for minimization of compliance C , with a constraint on the area fraction, is conventionally defined as

$$\min_{\rho} C = \mathbf{u}^T \mathbf{K} \mathbf{u}, \quad \text{s.t.} \frac{1}{A_{\Omega}} \sum_{e=1}^N \rho_e A_e \leq A, \quad (1)$$

where \mathbf{K} is the material stiffness matrix, \mathbf{u} is the vector of displacements, A_{Ω} is the total area of the domain, ρ_e is the density of element e , A_e is the area of each element, and A is a specified total area fraction. Here \mathbf{u} is related to the vector of applied loads, \mathbf{f} , through the relation

$$\mathbf{K} \mathbf{u} = \mathbf{f}. \quad (2)$$

Compliance is minimized, or, equivalently, stiffness maximized, to minimize the displacement undergone by the structure in response to loading. Minimizing compliance alone produces a structure primarily consisting of thick rods aligned with the principal direction of loading [Fig. 1(a)]. Hence, an anisotropic architecture can give rise to increased stiffness when the elements (trabeculae) are preferentially aligned with the loading direction.

However, trabecular bone does not consist of thick parallel rods. The surface of trabecular bone is necessary for its remodeling cycle, which requires contact with surrounding bone marrow for new osteoclasts to form [5]. Bone is resorbed by osteoclasts, with new bone deposited on the surface by osteoblasts. Trabecular bone also has a much higher surface area compared to cortical bone and, consequently, a large number of pores that hold marrow, nerves, and blood vessels.

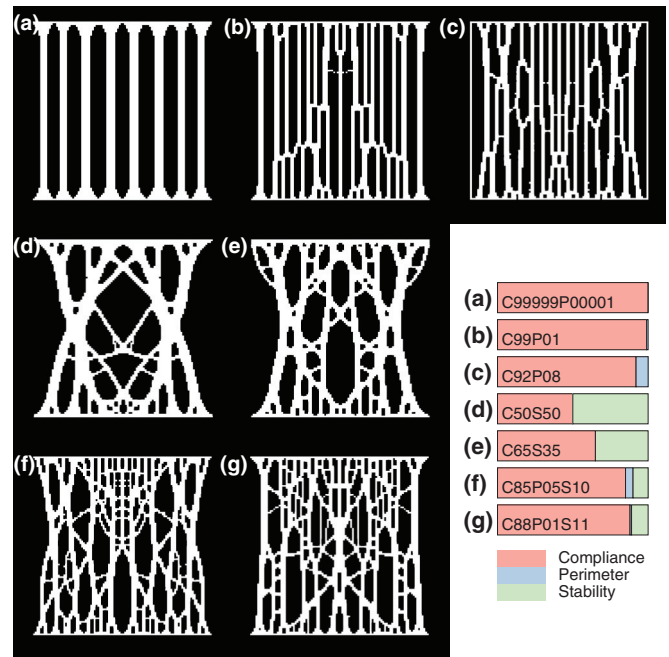


FIG. 1. Example 2D topology-optimized structures generated by varying objective weights. The horizontal bar plot in the lower right shows the relative weights assigned to the compliance, perimeter, and stability objectives for each image. Weights sum to 1. Panels (a)–(g): C99999P00001, C99P01, C92P08, C50S50, C65S35, C85P05S10, and C88P01S11, respectively. A total of 12 structures were generated for each of the seven parameter sets shown here; all structures for each parameter set are shown in the Supplemental Material [9].

Reverse-engineering trabecular bone to produce a structure of similar flexibility and lightness will require taking perimeter into account as in the objective function. Here we define P , the perimeter (2D) or surface area (3D) of the structure, in a dimension-agnostic form as

$$\max_{\rho} P = \int \Delta \rho \, d\Omega, \quad (3)$$

where ρ is the material density or volume at any point in the structure. Numerically, this translates to a sum of density changes across all element boundaries. Setting the perimeter function weight to a nonzero value and optimizing for both compliance and perimeter, while keeping the same volume, results in a structure with a greater number of thinner struts rather than fewer, thicker ones. Most of these thin struts are aligned in the principal loading direction, while a few are transverse.

Previous studies applying topology optimization to explore trabecular bone structure have considered only compliance as an objective function and included a perimeter constraint [6,7]. However, depending on the weights used, including only compliance (and perimeter) objective functions can result in an unstable model, such as one that consists of long, thin vertical rods. The stability of this model is represented by its critical buckling load, $P_{\text{crit}} = \max_{i=1, \dots, N_{\text{dof}}} P_i$. The objective in this case is to maximize the critical buckling load, and hence the stability, defined by the generalized eigenvalue

equation

$$\left[\mathbf{G}(\mathbf{u}) - \frac{1}{P_i} \mathbf{K} \right] \Phi_i = 0, \quad i = 1, \dots, N_{\text{dof}}, \quad (4)$$

where $\mathbf{G}(\mathbf{u})$ is the geometric stiffness matrix and Φ_i is the eigenvector associated with the i th buckling load. To avoid degeneracy of the eigenvalues $1/P_i$, which can result in poor or incorrect convergence of the optimizer, we apply a bound formulation [1] such that the stability optimization problem is written as

$$\begin{aligned} \min_{\rho} \beta, \quad \text{s.t. } \alpha^i \left(\frac{1}{P_i} \right) \leq \beta, \quad i = 1, \dots, N_{\text{dof}}, \\ \left[\mathbf{G}(\mathbf{u}) - \frac{1}{P_i} \mathbf{K} \right] \Phi_i = 0, \quad i = 1, \dots, N_{\text{dof}}, \end{aligned} \quad (5)$$

where α is a number slightly less than 1, e.g., 0.95, which ensures that each eigenvalue is slightly larger than the next. Note that this bound formulation will only actively impact eigenvalues near one end of the eigenvalue spectrum and eigenvalues in the interior or near the other end of the spectrum will inherently satisfy the constraint. As a result, we can safely truncate the series from N_{dof} (the total number of degrees of freedom in the system) terms to a much smaller number such as $n = 10$. Optimizing for stability as well as compliance and perimeter further increases the number of struts as well as those oriented at a nonzero angle to the primary loading (vertical) direction.

The multiple objectives are combined as a weighted sum, where the weights can be varied to change the relative importance of each objective [8]:

$$\begin{aligned} \min_{\rho} w_1 C_0 - w_2 P_0 + w_3 \beta_0, \\ \text{s.t. } \alpha^i \left(\frac{1}{P_i} \right) \leq \beta, \quad i = 1, \dots, N_{\text{dof}}, \\ \left[\mathbf{G}(\mathbf{u}) - \frac{1}{P_i} \mathbf{K} \right] \Phi_i = 0, \quad i = 1, \dots, N_{\text{dof}}, \\ \frac{1}{A_{\Omega}} \sum_{e=1}^N \rho_e A_e, \quad \sum_{i=1}^3 w_i = 1, \end{aligned} \quad (6)$$

where w_i are the respective weights on each of the objective functions C_0 , P_0 , and β_0 , which refer to normalized compliance, perimeter, and stability, respectively [Eqs. (1), (3), and (6)]. Here we normalize by independently optimizing for each of the objectives separately and then evaluating each objective function on each optimized structure. The functions are then normalized relative to the maximum and minimum values across each of the structures.

Note that the purpose of normalization is to make the magnitude of each function more consistent. As a result, the actual values of the function weights for one system are somewhat arbitrary in that they depend on the normalization procedure used. As such, the weights are only truly meaningful when compared relative to each other or across different optimization problems. It is possible, once the optimization is completed, to compute the actual contribution of each objective to the aggregate cost function; examples are included in the Supplemental Material [9].

To load the material in the design domain we apply an equal compressive force to the top and bottom of the domain to simulate the loading condition of trabecular bone. Weak springs are also attached to the nodes at the bottom of the domain to eliminate rigid-body modes without significantly affecting structural response. As the loading conditions and design domain are perfectly symmetric, we also enforce symmetry of the design to prevent small numerical errors from introducing arbitrary asymmetry into the design. While true trabecular bone is not symmetric, this asymmetry can be attributed to more complex loading patterns and minor material defects within the bone, the effects of which are not considered here.

We generate topology-optimized structures for a total of seven different sets of objective weights. One example structure for each parameter set is shown in Fig. 1; all remaining structures are included in the Supplemental Material [9]. Each set contains 12 different structures. Each structure is generated from the same initial density distribution, with a small perturbation added to ensure that each optimization with the same weights will converge to a different structure. We label each set of structures with the letters C, P, or S, representing compliance, perimeter, and stability objectives, respectively, followed by the corresponding weight (times 100) of the objective function used to generate the structures.

Figure 1(a) is an example structure from the set labeled C99999P00001, which is representative of optimizing all but entirely for compliance. The weight of the compliance function is 0.99999 rather than 1 even. If the compliance weight were 1, for some initial conditions, then it is possible that the result would be a contiguous piece of material with no porosity. Hence, we assign a very small weight of 0.00001 to the perimeter objective; combined with the different initial conditions, this promotes variation in topology. Stability is not considered in this case.

Figures 1(b) and 1(c), labeled C99P01 and C92P08, respectively, are generated by including weights for both compliance and perimeter, resulting in an increased number of thinner struts and consequently a greater number of pores.

Figures 1(d) and 1(e), labeled C50S50 and C65S35, respectively, are generated by including weights for compliance and stability but omitting the perimeter objective. The resulting structures consist of much thicker struts that are largely oriented at an angle to the vertical. The structures are also noticeably concave at each side.

Figures 1(f) and 1(g), labeled C85P05S10 and C88P01S11, respectively, are generated from combining all three objectives. These structures contain more struts and small pores than the other sets, with a few longer vertical columns joined by a number of shorter angled elements.

III. NETWORK MODELING AND MECHANICAL SIMULATION

A. Skeletonization

From topology-optimized images, we generate graph models, following Ref. [3], that allow us to utilize existing graph theoretical methods to efficiently analyze the topology of networked structures. Converting a topology-optimized structure

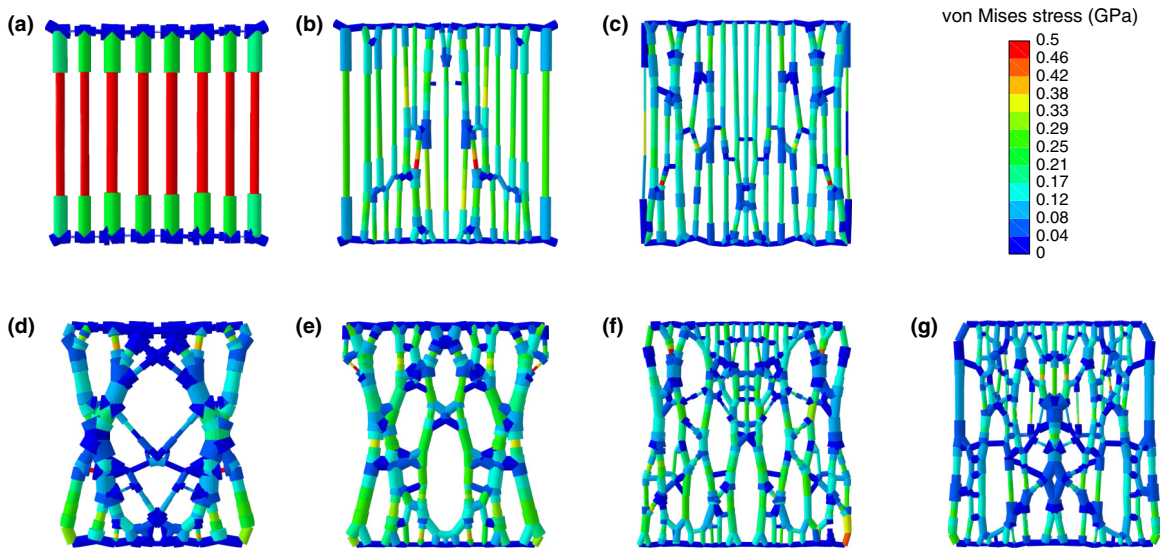


FIG. 2. Example beam element models. Color of beams represents spatial distribution of von Mises stress in example structures for each parameter set. Each model is shown at the timestep immediately preceding the first element failure in each respective simulation. (a) C99999P00001, (b) C99P01, (c) C92P08, (d) C50S50, (e) C65S35, (f) C85P05S10, and (g) C88P01S11.

to a graph begins with skeletonization: the “skeleton” of each image is determined by progressively thinning the image until its medial axis, a one-pixel-wide line running through the center of the network, is found. This medial axis, or skeleton, is then converted to a graph by setting nodes at branch points where three or more struts meet, with edges corresponding to struts themselves. The edges are weighted according to the respective average thicknesses of corresponding struts. Skeletonization and graph conversion are accomplished using the Skeleton3D and Skel2Graph toolboxes for MATLAB [10]. Strut thicknesses are computed using the BoneJ plug-in [11] for ImageJ (National Institutes of Health, Bethesda, MD).

B. Beam element models

To simulate mechanical loading and deformation, we translate these graphs into streamlined finite-element models. Rather than meshing the trabecular model, we generate beam-element models from the graphs, where each link is represented by a Timoshenko beam with a uniform thickness corresponding to its weight (Fig. 2). Nodes in the beam-element model correspond directly to nodes in the network. The beam material is defined by an elastic modulus of 10 GPa and a Poisson ratio of 0.16, following similar values as reported in the literature for bone [12,13].

Mechanical loading is simulated with Abaqus FEA (Dassault Systèmes, Vélizy-Villacoublay, France). The beam-element model is compressed from the top and bottom, representing loading along the superior-inferior direction, the primary loading axis in vertebrae. The von Mises stress at each link is computed at each time step, along with the force and displacement of each node.

We solve the models in the linear-elastic regime, where the stress is linear as a function of strain. We also model failure by setting von Mises stress as a failure criterion; when the stress in a beam reaches the critical stress value, the beam is said to have failed and is removed from the simulation. The system

continues to be loaded even as beams fail and are removed. We arbitrarily set the failure criterion to be a von Mises stress of 0.5 MPa; as the response is linear, this value can be scaled up or down with no qualitative change in the overall behavior.

We note that the skeletonization and network conversion process is limited by its inability to fully capture nonuniform trabecular thicknesses or increased bulk at branch points (nodes). This trade-off, however, greatly simplifies modeling and provides a streamlined approach to relating topology with mechanics. To improve the resolution of trabecular thickness in beams with nonuniform widths, we divide longer beams into five segments, such that each segment can have a different thickness.

C. Bulk force-displacement response

Force-displacement curves for the seven beam-element models generated from the topology-optimized structures (Fig. 1) are compared in Fig. 3. We model the structures in the linear-elastic regime with a von Mises stress failure criterion. The force-displacement curves are hence linear until the initialization of beam failure, whereupon they exhibit large decreases until reaching zero, at which point the structure is said to have failed completely. As the first few beams fail, the system might be able to redistribute the load (and the force increases) until sufficient beams have failed, resulting in an overall softening trend where the force drops until it reaches zero. The force-displacement response after reaching zero exhibits fluctuations that are artifacts of wave propagation in the simulation and are not considered in the analysis of the results. The curves in Fig. 3 are truncated where the reaction force reaches zero, and the full force-displacement curves for each model are included in the Supplemental Material [9].

On average, stiffness (the slope of the force-displacement curve in the initial linear regime) is greatest for C99999P00001, the parameter set for which compliance minimization was most highly weighted. However, C50S50

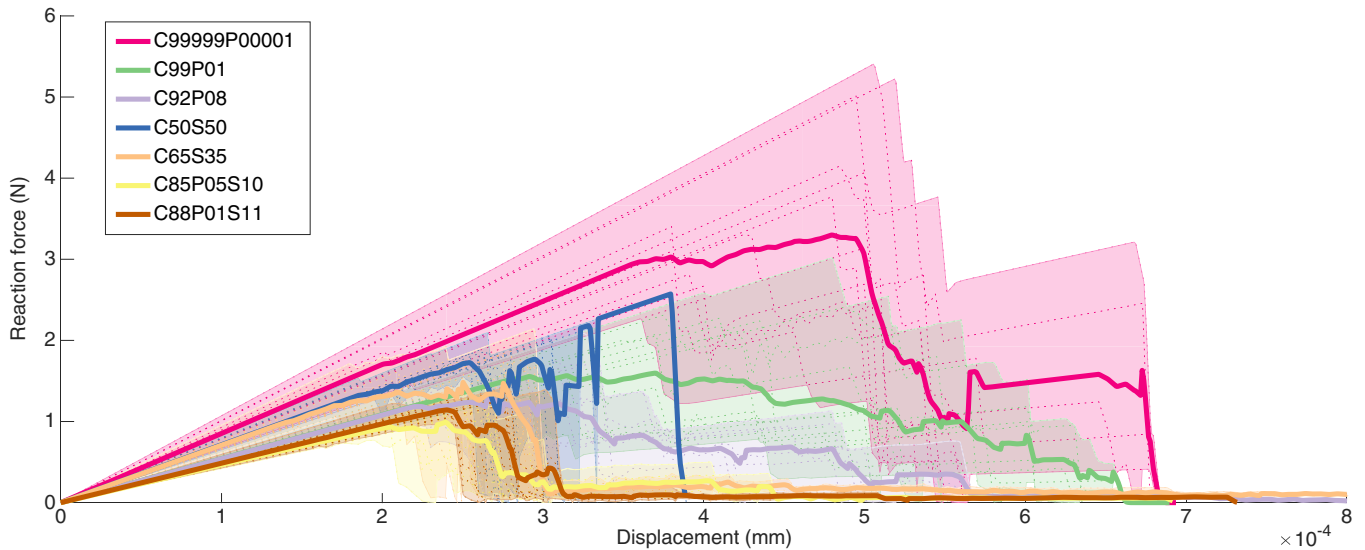


FIG. 3. Force-displacement response. The force-displacement curve for each structure is indicated by a thin dashed line; the average curve for each parameter set is shown as a thick solid line. Shaded areas represent the regions spanned by the highest and lowest reaction force for each parameter set.

and C65S35 demonstrate slightly higher average stiffness than C99P01 and C92P08, which have greater compliance minimization weights. The models with lowest stiffness are C85P05S10 and C88P01S11.

We use two additional metrics to quantify mechanical response: the peak reaction force typically attained at the onset of element failure, and the maximum displacement at total system failure (when the reaction force reaches 0). The peak force represents the strength of the model, while the maximum displacement serves as a proxy for the ductility of the structure as it undergoes fracture. A large maximum displacement could indicate that stresses redistribute such that the entire structure does not fail immediately when the first failure occurs. The distributions of peak force and maximum displacement are compared in an Ashby plot in Fig. 4(a). The highest peak forces are given by C99999P00001, followed by C99P01, while the peak force for the other parameter sets are comparable. The maximum displacement varies greatly for some parameter sets, in particular C92P08, C65S35, C85P05S10, and C88P01S11, while the variation in displacement is considerably smaller for C99999P00001 and C50S50.

We note that while C99999P00001 demonstrates the highest peak forces, it also has the largest variation in peak force. Hence, slight variations in structure across models, despite being generated under the same optimization criteria, can result in significantly different mechanical response. To probe robustness, we perturb each structure slightly and subject them to the same loading conditions as the original models. For each model, each node is shifted in both x and y coordinates by a small random distance of order 1% of the length of the structure.

For the purposes of this paper, we define robustness as the relative change in peak force between the original and perturbed models: $(F_{\text{peak, original}} - F_{\text{peak, perturbed}})/F_{\text{peak, original}}$. Robustness is plotted against the stiffness of the original model in Fig. 4. In some cases, the perturbed model can exhibit a

greater peak force than the original model, indicated by a positive robustness score. We observe that C99999P00001, which demonstrated the greatest variation in peak force among original models, exhibits relatively low robustness, with large spread in stiffness values. C65S35 exhibits the greatest variation in robustness, with several instances in which the perturbed model was stronger than the original model. C50S50 shows slightly lower robustness than C65S35; C50S50 and C65S35 exhibit roughly similar stiffness values and are the second stiffest models after C99999P00001. C99P01, C92P08, C85P05S10, and C88P01S11 demonstrate similar stiffness and robustness.

We note that the C50S50 structures lie on an approximately 45° line in the Ashby plot shown in Fig. 4. This suggests that these structures achieve a delicate balance between strength and ductility in which both mechanical markers increase hand in hand. This property is similar to what has been reported for some biological materials with superior mechanical properties such as mollusk shell, spider silk, and bone [14,15].

Our results suggest that while assigning almost all weight to compliance minimization can produce structures that are on average stiffer and tougher, these structures can be prone to small perturbations in geometry or objective weights. Moreover, optimizing for compliance and perimeter without accounting for stability can result in structures that are less robust and less stiff than those generated by assigning considerable weight to stability maximization. We observe that some structures in the C50S50 and C35S65 families exhibit positive robustness where geometric imperfections may lead to an increase in their strength and stiffness. This suggests that assigning significant weight to stability may enhance mechanical response under uncertain conditions. However, structures with small weights on both perimeter and stability objectives remain weaker and less robust than those for which perimeter is not considered.

We also include a set of “topological” Ashby plots (Fig. 5) that compare the robustness with network properties of each

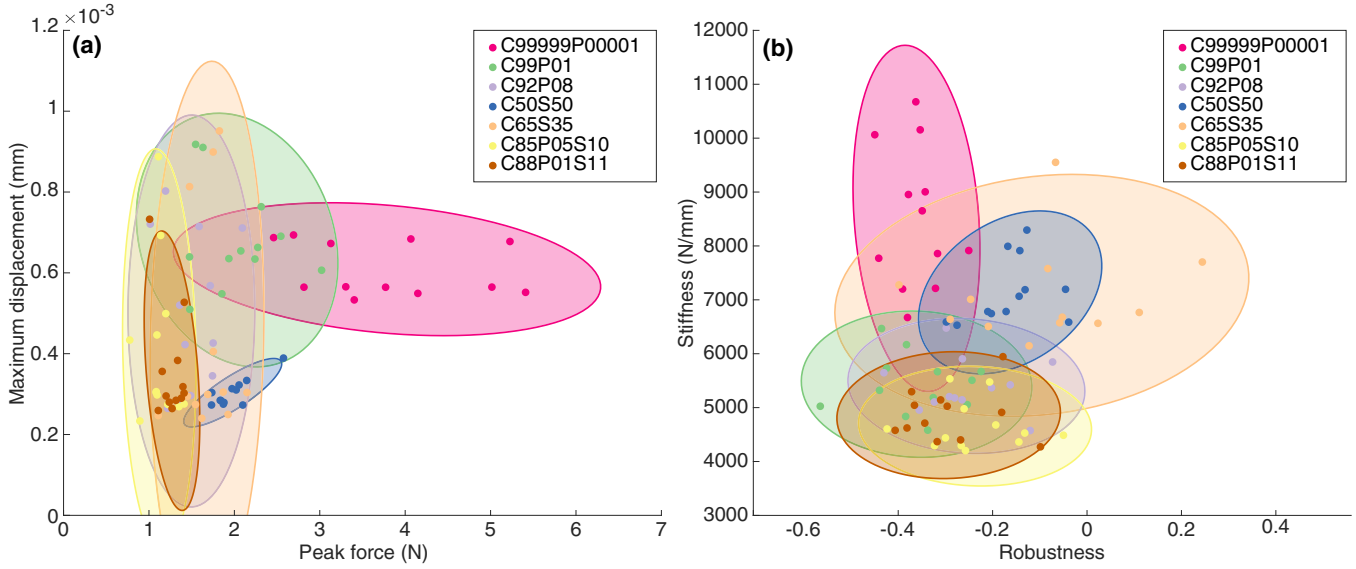


FIG. 4. Ashby plots comparing properties of different optimization parameter sets. Panel (a) compares the maximum displacement before complete failure with the peak reaction force attained. Panel (b) compares stiffness, the slope of the force-displacement curve in the linear regime prior to failure, with robustness, measured as the relative change between the peak forces of the original and perturbed models. Shaded ellipses represent 2σ confidence intervals.

model: average degree, average link thickness (corresponding to the average link weight without normalization), modularity, and the clustering coefficient. Modularity is a measure that describes how easily a graph can be partitioned into modules, or communities, where nodes within a community are densely connected to each other but sparsely connected to other nodes

in the network. Modularity is defined in Eq. (7) in the context of our application of community detection to characterizing failure. The null model used is given in Eq. (9). The clustering coefficient is defined as 3 times the number of triangles in a network (a set of three nodes connected by three edges) divided by the number of connected triples (three nodes connected by at least two edges) [16].

We observe that C99999P00001 has the lowest average degree, as would be expected due to the models consisting primarily of vertical columns, while C85P05S10 and C88P01S11, which have considerably more complicated architecture, have higher average degree. We observe only a weak correlation between degree and robustness (Pearson correlation coefficient $r = 0.23$, $p = 0.04$). We also observe a weak correlation between average link thickness and robustness ($r = 0.40$, $p < 0.001$). While the models vary greatly in modularity, with C99999P00001 the least modular and C85P05S10 and C88P01S11 the most, they do not exhibit large variation in clustering coefficient. We do not observe significant ($p < 0.05$) correlations between robustness and clustering coefficient and between robustness and modularity. Despite this, we discuss in Sec. III E how modularity and community structure can inform failure locations in a network.

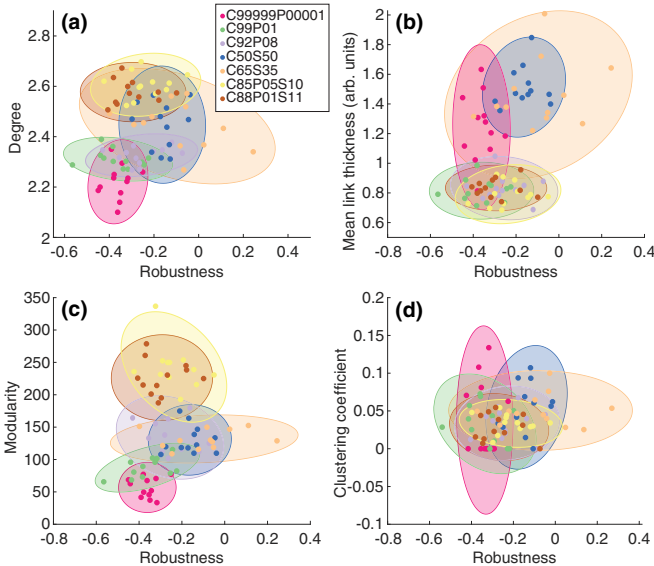


FIG. 5. Ashby plots comparing robustness and network properties. Robustness is defined as the relative change between the peak forces of the original and perturbed models. Panel (a) compares the average degree of each model with its robustness; panel (b) plots the mean link thickness (in arbitrary units); panel (c) plots the modularity [see Eq. (7) with null model given in Eq. (9) and resolution parameter $\gamma = 1.6$]; and panel (d) plots the clustering coefficient. Shaded ellipses represent 2σ confidence intervals.

D. Stress distribution

The fragility of these structures may be linked to the spatial distribution of stress: whether the stress is distributed relatively evenly or concentrated in a few beams. The distribution of (von Mises) stress across beams can vary greatly between parameter sets, as visualized in Fig. 2. Figure 6 illustrates the distribution of stress, normalized to the highest stress value in one beam in each model, averaged over all models in a set (histogram). In the models without stability objectives (top row), a large area fraction exhibits no stress, demonstrated by

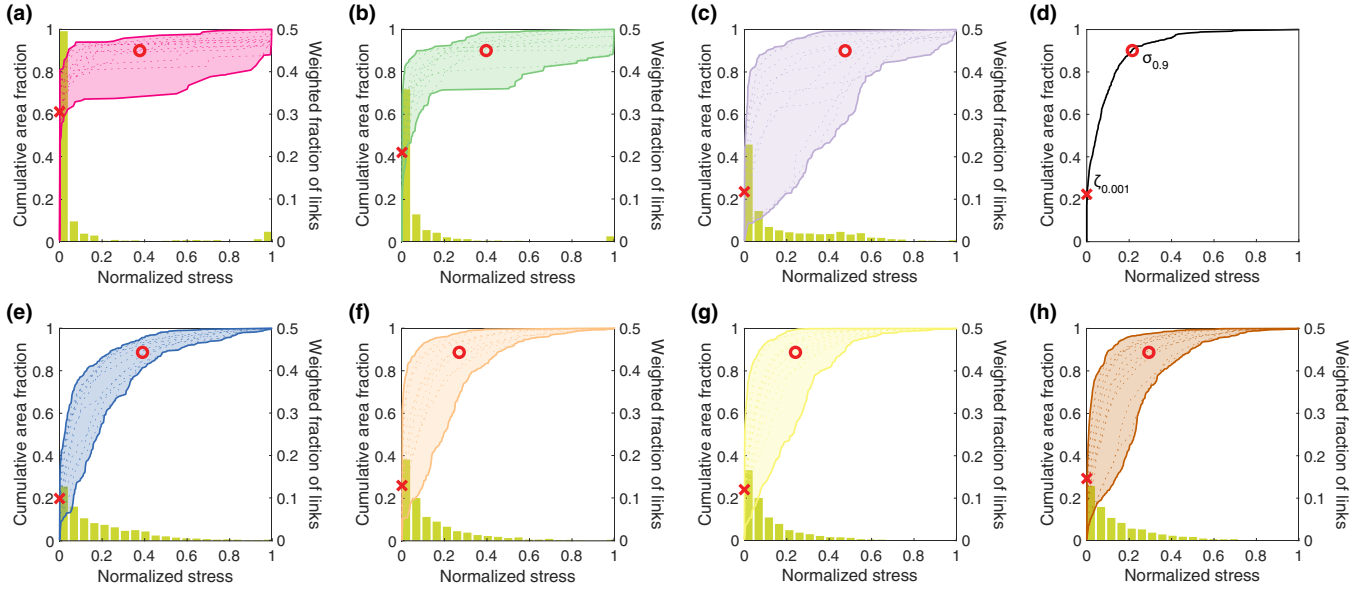


FIG. 6. Stress distributions. (a) C99999P00001, (b) C99P01, (c) C92P08, (d) example cumulative stress distribution, (e) C50S50, (f) C65S35, (g) C85P05S10, and (h) C88P01S11. Histograms represent the average distribution of normalized stress for each parameter set, weighted by the thickness of each link. The shaded regions illustrate the variation in the cumulative distribution of normalized stress, expressed in terms of the fraction of area occupied by the links (normalized by the area of the entire model). Dotted lines within the shaded regions correspond to the distributions of each individual model. Red crosses represent average $\zeta_{0.001}$ and $\sigma_{0.9}$ for each parameter set, as illustrated by the example in panel (d).

a considerable peak at 0. The distribution for C99999P00001, however, shows that in some models, a small fraction of links bears almost all of the stress. In contrast, the models with stability objectives (bottom row) demonstrate a peak at 0 with relatively heavy tails.

Figure 6 also shows the cumulative fraction of beams that bear normalized stress values between 0 and 1 (colored shaded regions). For C99999P00001 and, to a lesser extent, C99P01, a notable fraction of beams have normalized stress close to 0. Their cumulative distributions rise sharply compared to those with stability objectives before flattening out. To quantify the stress distribution, we compute two metrics, $\zeta_{0.001}$ and $\sigma_{0.9}$. $\zeta_{0.001}$ is the fraction of total area with normalized stress less than or equal to 0.001, and $\sigma_{0.9}$ is the normalized stress value such that 90% of the total area bears stress less than or equal to this value; similar metrics were previously defined in the context of trabecular bone in Ref. [3]. Average values for $\zeta_{0.001}$ and $\sigma_{0.9}$ are shown in Table I. $\zeta_{0.001}$ is highest for C99999P00001; approximately 61% of the total area—corresponding to 67% of beams—bear almost no stress, followed by C99P01 at 42% (52% of beams). For the remaining models, which all include stability weights except for C92P08, $\zeta_{0.001}$ is lower, representing between 16% and 26% of area that is unstressed, indicating that stress is distributed more evenly for these models.

For $\sigma_{0.9}$, the highest values are found for the three models with the highest compliance weights. These models have relatively high $\zeta_{0.001}$ values as well, thus containing a larger percentage of low-stress area with the stress more evenly distributed on the remaining elements. $\sigma_{0.9}$ is moreover relatively high for C50S50, which also has a low $\zeta_{0.001}$ value, indicating that the stress distribution is less skewed. Overall, $\sigma_{0.9}$ ranges between 0.24 and 0.47 for all

models, implying that a small percentage of beams bear large stresses.

The models with stability objectives are most similar in visual resemblance to trabecular bone. The two models with all three objective weights, C85P05S10 and C88P01S11, have the highest degrees of all models. We also apply the metric of z orientation previously defined in Ref. [3], a value between 0 and 1 that describes the preferred orientation of struts (where 0 is transverse to the vertical direction and 1 is parallel), as well as the weighted z orientation, where the z orientation of each link is weighted proportionally to its thickness. We observe that while the average z orientation of the topology-optimized structures ranges between 0.64 and 0.83, much higher than the average values observed for bone (close to 0.5), C85P05S10 and C88P01S11 have the lowest weighted z orientation, indicating that less mass is distributed in vertical columns compared to, for example,

TABLE I. Average $\zeta_{0.001}$ and $\sigma_{0.9}$ values for each set. $\zeta_{0.001}$ gives the fraction of beams with normalized stress less than or equal to 0.001, and $\sigma_{0.9}$ gives the normalized stress value wherein 90% of beams bear stress less than equal to this value. Stress is normalized to the largest stress value in a single beam in each individual structure.

Set	$\zeta_{0.001}$	$\sigma_{0.9}$
C99999P00001	0.612	0.378
C99P01	0.421	0.397
C92P08	0.236	0.475
C50S50	0.199	0.391
C65S35	0.260	0.270
C85P05S10	0.187	0.241
C88P01S11	0.162	0.293

the models with high compliance weights and no stability objective. However, direct comparison between the topology-optimized structures and bone are limited by the 2D nature of the topology-optimized structures and the 3D nature of the bone volumes, as well as the different sample sizes (the bone volumes contain over an order of magnitude more elements than the topology-optimized structures).

For the models with stability objectives, the shape of their stress distributions is also the most similar to that of bone [3]. For the topology-optimized models, however, $\zeta_{0.001}$ remains much lower than for bone, which is on average approximately 0.43 [3], while this value is surpassed for C99999P00001 and C99P01. For bone, approximately 6.7% of the total volume fraction bears less than 90% of the normalized stress [17], indicating that the stress distributions are considerably less skewed for the topology-optimized models than for bone—note, however, that the topology-optimized structures generated here are two dimensional, while the bone volumes analyzed previously are three dimensional.

E. Community detection

We use community detection to investigate whether the topology of the network encodes information about likely points of failure. We observe that locations of failure—i.e., the most stressed beams in the finite-element models—do not generally correspond with the thinnest elements, and there is no preferred orientation associated with the failed beams. We hypothesize that elements corresponding to links that connect two different communities—“boundary links”—are more likely to fail than elements within a community.

Community detection is a method of determining clusters (communities) that contain dense within-cluster connections, with sparse connections to the rest of the network [16]. The development of community detection algorithms and their application as a beginning phase of network structure or function diagnostics is a focus of network science [18]. Community detection has been used to characterize social interactions, brain function, and much more but most pertinently to characterize force chains in granular materials [19,20]. Granular packings have been described by assigning nodes to individual particles and edges to contact forces between particles [21]. Community detection can extract information about force chains, networks that typically resemble interconnected filaments primarily aligned with the principal axes of loading.

Here we perform community detection to identify whether failure locations reside in any particular locations within the network topology. Community detection typically involves maximizing a modularity function Q that identifies community structure relative to a null model P [16,21]:

$$Q = \sum_{ij} [W_{ij} - \gamma P_{ij}] \delta(g_i, g_j), \quad (7)$$

where W_{ij} is the weight of the edge between nodes i and j , γ is a resolution parameter that controls community size, P_{ij} specifies the expected weight of the edge between nodes i and j under the null model, g_i is the community assignment of node i , and $\delta(g_i, g_j)$ is the Kronecker δ .

The null model is commonly chosen to be a random rewiring of nodes with the degree distribution kept constant

(Newman-Girvan null model):

$$P_{ij} = \frac{s_i s_j}{2m}, \quad (8)$$

where s_i is the weighted degree of node i and m is the sum of all edge weights in the network (i.e., $m = \frac{1}{2} \sum_{ij} W_{ij}$). This null model assumes that connections between any pair of nodes is possible. However, because the networks are spatially embedded, and long-range connections that span large spatial distances are impossible, we choose a *geographical null model*, initially developed for use in the study of brain networks and subsequently adapted for granular networks [19]:

$$P_{ij} = \rho B_{ij}, \quad (9)$$

where ρ is the mean edge weight of the network and \mathbf{B} is the binary adjacency matrix of the network (i.e., the adjacency matrix where all nonzero edge weights have been set to 1).

The geographical null model produces communities that are anisotropically aligned with the vertical direction and thus reminiscent of force chains. The resolution parameter γ modulates the size and number of communities. We set γ to 1.6. Examples of community structure are shown in Fig. 7.

We observe that failures tend to occur at the boundaries between communities, i.e., in links that connect two different communities. We note that our choice of γ is intended to result in community structure that is most informative at characterizing failure locations. If γ is too small, then the community structure may contain too few communities, to the limit of 1, and if γ is too large, each node can be considered its own community. At both extremes, it will not be possible to observe how the modularity of the network plays a role in influencing failure.

We quantify statistical significance with the Bayes factor, which represents the inverse of the ratio of probability of the data given the null hypothesis—where the probability q of a failure occurring at a boundary link is equal to the fraction of boundary links in the network l_{bd}/L —to the probability of the data given the alternative hypothesis—where the probability q of failure occurring at a boundary link is unknown and where we assume a uniform prior on $[0,1]$. The Bayes factor is given by

$$\text{BF} = \frac{P(F_{bd} = f | F_{tot}, q \text{ unknown})}{P(F_{bd} = f | F_{tot}, q = l_{bd}/L)}, \quad (10)$$

where F_{bd} is the number of failures at boundaries, F_{tot} is the total number of failures, l_{bd} is the total number of boundary links, and L is the total number of links. Furthermore,

$$P(F_{bd} = f | F_{tot}, q = l_{bd}/L), \quad (11)$$

$$= \binom{F_{tot}}{f} (l_{bd}/L)^f (1 - l_{bd}/L)^{F_{tot}-f}, \quad (12)$$

and

$$P(F_{bd} = f | F_{tot}, q \text{ unknown}), \quad (13)$$

$$= \binom{F_{tot}}{f} \int_0^1 q^f (1 - q)^{F_{tot}-f}, \quad (14)$$

$$= \binom{F_{tot}}{f} \mathbf{B}(f + 1, F_{tot} - f + 1), \quad (15)$$

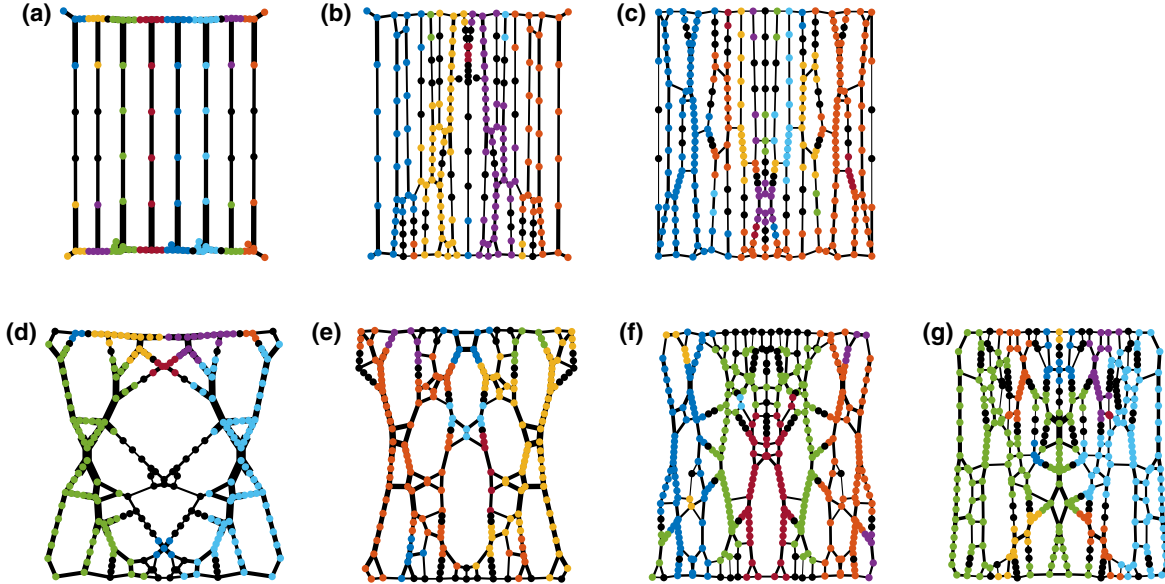


FIG. 7. Example of community structure for each parameter set. (a) C99999P00001, (b) C99P01, (c) C92P08, (d) C50S50, (e) C65S35, (f) C85P05S10, and (g) C88P01S11. Nodes are colored to distinguish between communities. Black nodes represent communities of one node.

where B is the beta function. Then the Bayes factor is given by

$$\text{BF} = \frac{B(f+1, F_{\text{tot}} - f + 1)}{(l_{\text{bd}}/L)^f (1 - l_{\text{bd}}/L)^{F_{\text{tot}} - f}}. \quad (16)$$

If $\text{BF} > 10^2$, or similarly $\ln \text{BF} > 5$, then the evidence strongly supports the alternative hypothesis over the null hypothesis.

We find that the fraction of failures that occur at these boundary links ranges between 0.58 and 0.73 for structures in sets C50S50, C65S35, C85P05S10, and C88P01S11. The fractions are smaller for the sets without stability objectives and decrease as the compliance weight increases. In contrast, the fraction of links in the networks that are boundary links ranges between 0.25 and 0.32.

The average values of F_{bd} , l_{bd}/L , and $\ln \text{BF}$ are shown in Table II, while their distributions are illustrated in Fig. 8. The Bayes factors are lowest for C99999P00001 and C92P08. Moreover, the spread of F_{bd} values for C99999P00001 and C92P08 are the largest, with some structures having very few failures at boundaries in the case of C99999P00001. We

TABLE II. Fraction of failures that occur at boundaries between communities (F_{bd}) and overall fraction of edges that join two different communities (l_{bd}/L). Logarithm of Bayes factor > 5 indicates statistical significance.

Set	F_{bd}	l_{bd}/L	$\ln \text{BF}$
C99999P00001	0.359	0.255	12.6
C99P01	0.469	0.264	25.9
C92P08	0.517	0.265	19.6
C50S50	0.724	0.321	43.0
C65S35	0.733	0.324	43.6
C85P05S10	0.576	0.279	49.6
C88P01S11	0.722	0.283	96.0

observe that models with high compliance weights and no stability objective contain a greater number of vertical beams and are less disordered in structure, which can result in community detection being less useful at characterizing failure locations. Overall, the Bayes factors indicate that failures are significantly more likely to occur at a boundary link (to about 70% of links) compared to the fraction of links that form boundaries (about 30% of links). This suggests that failure locations are not randomly distributed across a network but are likely to be associated with the underlying topology.

IV. DISCUSSION

We use multiobjective topology optimization to generate networked structures inspired by trabecular bone. An analysis of the stress distribution and fracture patterns in these structures reveals the contribution of compliance, perimeter, and stability objectives to strength and resilience. We observe that in structures with the greatest weight maximizing stiffness, with little to no consideration given to optimizing for stability, mechanical response is sensitive to small geometric perturbations. In comparison, structures generated with greater weight given to the stability objective are more robust.

Each topology-optimized structure analyzed in this paper is constrained to have the same area fraction, but mechanical response can vary widely among structures that otherwise have the same objective weights. This corroborates previous findings that bone mass density is an incomplete predictor of fracture resistance in trabecular bone [22–26]. Moreover, this variation is most notable for structures optimized primarily for compliance. Prior studies of topology-optimized structures inspired by trabecular bone involve solely compliance minimization with perimeter constraints [6,7]. Here we find that when perimeter and stability weights are taken into account, the reaction force and displacement maxima shift significantly. This may suggest that compliance minimization alone overestimates the behavior of a realistic biological

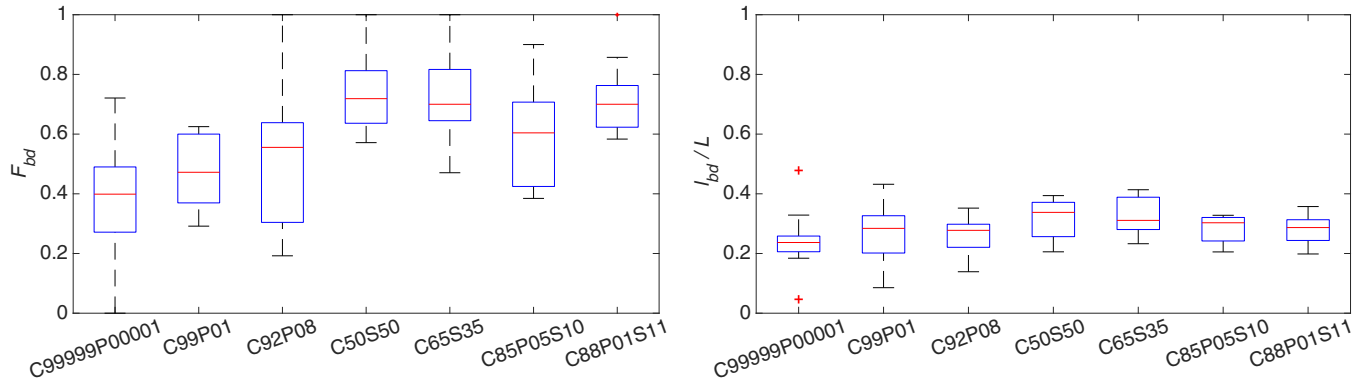


FIG. 8. Variation in fraction of failures that occur at boundaries between communities (F_{bd}) and overall fraction of edges that join two different communities (l_{bd}/L).

material. Since these materials are typically multifunctional, introducing multiple objectives beyond compliance in topology optimization will provide more flexibility in balancing various trade-offs without greatly compromising the mechanical response. When considered on its own as a design principle, Wolff’s law, which states that bone adapts itself to resist the loads under which it is placed, and hence typically results in increased bone mass along principal loading axes, may result in structures that are less robust. In real biological tissues, Wolff’s law is likely not the sole factor governing remodeling processes, and it may hence be important to use robustness as an objective for bioinspired design.

The topology optimization algorithm used here is not a remodeling algorithm that takes into account either strain-signal or constant resorption-deposition behavior (e.g., Refs. [27,28]), but future work can consider the remodeling processes that depend on local considerations and influence how bone changes as it ages. While we do use global objective functions to more efficiently generate the structures, the optimizer still makes the decision to add or remove material from a given location on a semilocal basis. Specifically, the global compliance function can be rewritten as a sum of strain energies for each element in the mesh. To minimize this, it has been our experience that the optimizer will seek a structure that reduces strain consistently across all elements. This does not necessarily preclude the development of a small number of local stress concentrations, but it does mean that the developed structure will have a minimal average strain across all elements when subjected to the prescribed load. Moreover, other objective functions or constraints that seek to minimize or bound a local measure of stress, such as von Mises stress or the maximum principal stress, may be considered in future work.

It will be valuable to draw further biological inspiration from the changes in bone structure that occur due to aging. As bone ages, trabecular architecture increases in anisotropy; trabeculae that are transverse to the principal loading direction are preferentially resorbed, and those that are parallel become thicker [22,29]. Currently, our topology-optimization results are static and the objectives used are not chosen with regard to a material that undergoes age-related geometric changes. Additional insight into aging processes can be achieved by extending the modeling procedure to begin with our original topology-optimized structures as initial conditions, followed

by an optimization process that reflects the conditions of aging bone.

Our mechanical simulations in this paper are linearly elastic, followed by brittle failure initiated by a stress-based criterion. An entire beam fails at once when the stress in the beam reaches a specified threshold, but in bone, the nonuniform thicknesses of trabeculae would result in beams that fail progressively. Our division of each beam into five segments serves to mitigate this discrepancy. Moreover, taking into account inelasticity and subscale energy dissipation mechanisms can improve realistic modeling of bonelike structures.

Our observation of substantial variation in the distribution of stress across different models suggests an investigation into the extent to which topology optimization can engineer redundancy in structures. A structure with redundant or sacrificial beams may have higher toughness as the failure of some beams might not immediately result in catastrophic system failure, and stress can be redistributed through remaining beams.

In this paper, we introduce a community detection approach for characterizing fracture locations which is inspired by prior studies of force chains in networks derived from granular packings. We observe that, for an appropriate choice of resolution parameter, the fraction of failures occurring at links which connect different communities are significantly greater than the fraction of links that are boundaries. This suggests an association between boundaries and failure locations, and our results are consistent with the observations of Berthier *et al.*, who have used edge betweenness centrality to predict locations of failure in experimental 2D disordered networks [30]. Edge betweenness centrality is a measure that describes the frequency at which an edge lies on the shortest path between pairs of nodes in a network. Indeed, edge betweenness centrality as a failure marker is akin to our use of boundary links in characterizing failure locations as calculating edge betweenness can be used for determining community structure as per the Girvan-Newman method [31]. Edges connecting different communities have high edge betweenness centrality.

Future work will aim to potentially incorporate other factors alongside community structure to accurately predict locations of failure in a wide range of networked structures. In doing so, our methods are likely to be applicable across

domains and can be incorporated into a more comprehensive diagnostic tool for fracture susceptibility.

Overall, the modeling framework developed in this paper has wide-ranging applications for the design of materials and networked structures inspired by nature. While we focus on macroscale architecture in this work, engineering additional architecture at micro- and nanoscales can lead to improved function as bone, along with other naturally occurring materials, exhibits structure and mechanisms of strength at a range of scales [32,33]. At the microscale, bone tissue is composed of mineralized collagen fibrils embedded in an organic matrix, and the fibrils themselves comprise mineralized platelets staggered in a regular pattern within a collagen matrix [34]. Other naturally occurring materials such as nacre contain a similar architecture of elongated platelets organized periodically in a matrix [14]. Characterizing the contribution of multiscale organization to emergent strength can further inform the development of bioinspired materials.

ACKNOWLEDGMENTS

We thank Avik Mondal for contributions to the network modeling framework. This work was supported by the David and Lucile Packard Foundation, the Institute of Collaborative Biotechnologies through Army Research Office Grant No. W911NF-09-D-0001, and the National Science Foundation under Grants No. EAR-1345074 and No. CMMI-1435920. Use was made of computational facilities purchased with funds from the National Science Foundation (CNS-1725797) and administered by the Center for Scientific Computing (CSC). The CSC is supported by the California NanoSystems Institute and the Materials Research Science and Engineering Center (NSF DMR 1720256) at UC Santa Barbara. The content of the information does not necessarily reflect the position or the policy of the US government, and no official endorsement should be inferred.

-
- [1] M. P. Bendsøe and O. Sigmund, *Topology Optimization* (Springer, Berlin, 2003).
- [2] J. Wolff, P. G. J. Maquet (translator), and R. Furlong (translator), *The Law of Bone Remodelling* (Springer-Verlag, Berlin, 1986).
- [3] A. Mondal, C. Nguyen, X. Ma, A. E. Elbanna, and J. M. Carlson, *Phys. Rev. E* **99**, 042406 (2019).
- [4] D. Peetz, Multi-objective topology optimization for trabecular bone-like structure: Role of stability and surface area, Master's thesis, University of Illinois at Urbana-Champaign (2016).
- [5] E. Seeman and P. D. Delmas, *N. Engl. J. Med.* **354**, 2250 (2006).
- [6] C. Boyle and I. Y. Kim, *J. Biomech.* **44**, 935 (2011).
- [7] I. G. Jang and I. Y. Kim, *J. Biomech.* **41**, 2353 (2008).
- [8] Note that the weight w_2 on the perimeter objective is negative, since we aim to maximize perimeter while minimizing the other objectives.
- [9] See Supplemental Material at <http://link.aps.org/supplemental/10.1103/PhysRevE.100.042402> for a discussion of methodological considerations and images of all topology-optimized structures analyzed in this paper.
- [10] M. Kerschnitzki, P. Kollmannsberger, M. Burghammer, G. N. Duda, R. Weinkamer, W. Wagermaier, and P. Fratzl, *J. Bone Miner. Res.* **28**, 1837 (2013).
- [11] M. Doube, M. M. Klosowski, I. Arganda-Carreras, F. P. Cordelières, R. P. Dougherty, J. S. Jackson, B. Schmid, and J. R. Hutchinson, *Bone* **47**, 1076 (2010).
- [12] J. Y. Rho, R. B. Ashman, and C. H. Turner, *J. Biomech.* **26**, 111 (1993).
- [13] C. Jorgenson and T. Kundu, *J. Orthop. Res.* **20**, 151 (2002).
- [14] H. D. Espinosa, J. E. Rim, F. Barthelat, and M. J. Buehler, *Prog. Mater. Sci.* **54**, 1059 (2009).
- [15] U. G. K. Wegst, H. Bai, E. Saiz, A. P. Tomsia, and R. O. Ritchie, *Nat. Mater.* **14**, 23 (2015).
- [16] M. E. J. Newman, *Networks: An Introduction* (Oxford University Press, Oxford, 2010).
- [17] Note that the average values of $\zeta_{0.001}$ and $\sigma_{0.9}$ as reported in Ref. [3] are 0.410 and 0.136, which were determined with respect to a cumulative distribution over the number of links rather than volume fraction. As each link has a different volume, these values correspond to 0.428 and 0.067, respectively, when volume fraction is taken into account.
- [18] S. Fortunato and D. Hric, *Phys. Rep.* **659**, 1 (2016).
- [19] D. S. Bassett, E. T. Owens, M. A. Porter, M. L. Manning, and K. E. Daniels, *Soft Matter* **11**, 2731 (2015).
- [20] L. Papadopoulos, J. G. Puckett, K. E. Daniels, and D. S. Bassett, *Phys. Rev. E* **94**, 032908 (2016).
- [21] L. Papadopoulos, M. A. Porter, K. E. Daniels, and D. S. Bassett, *J. Complex Netw.* **6**, 485 (2017).
- [22] P. McDonnell, P. E. McHugh, and D. O'Mahoney, *Ann. Biomed. Eng.* **35**, 170 (2007).
- [23] S. A. Goldstein, R. Goulet, and D. McCubbrey, *Calcif. Tissue Int.* **53**, S127 (1993).
- [24] R. W. Goulet, S. A. Goldstein, M. J. Ciarelli, J. L. Kuhn, M. B. Brown, and L. A. Feldkamp, *J. Biomech.* **27**, 375 (1994).
- [25] M. L. Brandi, *Rheumatology* **48**, iv3 (2009).
- [26] A. J. Fields, S. K. Eswaran, M. G. Jekir, and T. M. Keaveny, *J. Bone Miner. Res.* **24**, 1523 (2009).
- [27] R. Huiskes, R. Ruimerman, G. H. van Lenthe, and J. D. Janssen, *Nature* **405**, 704 (2000).
- [28] R. Ruimerman, P. Hilbers, B. van Rietbergen, and R. Huiskes, *J. Biomech.* **38**, 931 (2005).
- [29] J. S. Thomsen, E. N. Ebbesen, and L. Mosekilde, *Bone* **31**, 136 (2002).
- [30] E. Berthier, M. A. Porter, and K. E. Daniels, *Proc. Natl. Acad. Sci. USA* **116**, 16742 (2019).
- [31] M. Girvan and M. E. J. Newman, *Proc. Natl. Acad. Sci. USA* **99**, 7821 (2002).
- [32] J. Y. Rho, L. Kuhn-Spearing, and P. Zioupos, *Med. Eng. Phys.* **20**, 92 (1998).
- [33] P. Fratzl and R. Weinkamer, *Prog. Mater. Sci.* **52**, 1263 (2007).
- [34] I. Jäger and P. Fratzl, *Biophys. J.* **79**, 1737 (2000).